

Article

Classification and Transition of Grassland in Qinghai, China, from 1986 to 2020 with Landsat Archives on Google Earth Engine

Pengfei He , Yuli Shi ^{*}, Haiyong Ding and Fangwen Yang

School of Remote Sensing and Geomatics Engineering, Nanjing University of Information Science and Technology, Nanjing 210044, China; gopfhe@nuist.edu.cn (P.H.); 002093@nuist.edu.cn (H.D.); 20211211025@nuist.edu.cn (F.Y.)

^{*} Correspondence: ylshi@nuist.edu.cn

Abstract: The lack of long-duration, high-frequency grassland classification products limits further understanding of the grasslands' long-term succession. This study first explored the annual mapping of grassland with fourteen categories at 30 m in Qinghai, China, from 1986 to 2020 based on Google Earth Engine (GEE) and the Integrated Orderly Classification System (IOCSG). Specifically, we proposed an image composite strategy to obtain annual source images for classification, by quarterly compositing multi-sensor and multi-temporal Landsat surface reflectance images. Subsequently, the 35-year area time series of each category was analyzed in terms of trend, degree of change, and succession of each category. The results indicate that the different grasslands of the IOCSG can be effectively differentiated by utilizing the designed feature bands of remote sensing data. Additionally, the proposed annual image composition strategy can not only decrease the invalid pixels but also promote classification accuracy. The grasslands transition analysis from 1986 to 2020 implies the progressive urbanization, warming, and wetting trend in Qinghai. The generated 35-year annual grassland thematic data in Qinghai can serve as an elementary dataset for further regional ecological and climate change studies. The proposed methodology of large-scale grassland classification can also be referenced to other applications like land use/cover mapping and ecological resource monitoring.

Keywords: alpine grassland ecosystem; grassland classification; grassland transition; Google Earth Engine



Citation: He, P.; Shi, Y.; Ding, H.; Yang, F. Classification and Transition of Grassland in Qinghai, China, from 1986 to 2020 with Landsat Archives on Google Earth Engine. *Land* **2023**, *12*, 1686. <https://doi.org/10.3390/land12091686>

Academic Editors: Kathryn Sheffield, Mohammad Abuzar and Alison L. Cowood

Received: 15 July 2023

Revised: 22 August 2023

Accepted: 25 August 2023

Published: 28 August 2023



Copyright: © 2023 by the authors. Licensee MDPI, Basel, Switzerland. This article is an open access article distributed under the terms and conditions of the Creative Commons Attribution (CC BY) license (<https://creativecommons.org/licenses/by/4.0/>).

1. Introduction

Grasslands are major terrestrial ecosystems on earth, occupying about 40% of Earth's land surface [1]. Grasslands deliver crucial ecosystem services such as biodiversity conservation, climate regulation, carbon recycling, and the sustainable development of society [2,3]. A grassland type refers to a highly abstract generalization of grassland plant populations and their combinations in different habitats [4]; the transition of grasslands is a synthetic action of anthropogenic disturbance and natural change, which is likely to alter the composition of plant species [5]. Therefore, being conscious of the long-term spatiotemporal distribution and transition of different grassland types is significantly helpful for a better understanding of regional and global change.

Grasslands in China occupy nearly 400 million hectares, accounting for 41.7% of the country's land area [6]. They are mainly distributed in the northern temperate region and the western alpine region. In particular, the grasslands in the alpine region have received enormous attention, since they are considered more ecologically fragile and sensitive to climate change [7]. With regard to the high species diversity of the grasslands in China, a commonly used classification system is the Integrated Orderly Classification System of Grassland (IOCSG) [6]. The IOCSG involves a hierarchy of three classification levels according to the grass habitat. At the first level, grasslands are grouped into nine classes based on an index of moisture and temperature, including alpine meadow (AM), alpine steppe (AS), alpine meadow-steppe (AMS), alpine desert (AD), lowland meadow (LM),

mountain meadow (MM), temperate steppe (TS), temperate desert (TD), and temperate desert-steppe (TDS). The other two levels progressively group the grasslands into subclass and types according to edaphic conditions and vegetation types, respectively. To understand the extent and distribution of different grassland classes, China has conducted three nationwide grassland resource survey projects since the 1950s. These projects relied on the extensive manual interpretation of remote sensing imagery and field surveys during the grass growing season, which is labor intensive and time consuming.

Over the past years, there has been a significant surge in the accessibility of satellite remote sensing data along with advancements in machine learning techniques. As a result, automated and semi-automated classification methods utilizing remote sensing data are emerging as crucial tools for large-scale land surface mapping. Numerous studies have employed remote sensing data with diverse spatial and temporal resolutions, such as the Moderate Resolution Imaging Spectroradiometer (MODIS), Landsat series, Sentinel series, etc. [8–10], wherein Landsat is the only satellite program that can provide fifty years' continuous data with high spatial resolution (30 m) and temporal resolution (16 days) [11,12]. Meanwhile, the development of the remote sensing community has facilitated easy access to open-source datasets and geoprocessing algorithms on web-based computing platforms. The Google Earth Engine (GEE) [13], an advanced computation cloud platform for geospatial data analysis, combines planetary-scale analysis capabilities with a multi-petabyte catalog of satellite imageries and products from the MODIS, Landsat series, and Sentinel series, etc. GEE has spawned lots of geographical research at regional and planetary scales over a long period of time, such as land use and land cover (LULC) mapping [14,15], grassland monitoring [16,17], cropping intensity mapping [18], analyzing the anthropogenic disturbances of the landscape [19], and exploring the spatiotemporal patterns of certain biological parameters [20,21].

Nevertheless, most research in terms of large-scale grassland classification has been devoted to distinguishing grasslands from other land cover classes. For example, there exist several popular global LULC mapping products at a scale of 30 m or 10 m with a broad classification system involving grasslands, trees, built up, bare lands, water, etc., such as Finer Resolution Observation and Monitoring of Global Land Cover (FROM-GLC) [22], Global Land 30 [23], European Space Agency (ESA) Land use and Land Cover (ESA LC) [24], and ESA World Cover [25]. Meanwhile, most grassland-specific classification studies merely considered a simple classification system with limited classes and focused on restricted geographical regions. For example, Xu et al. [4] conducted a study aimed at classifying grassland in a specific region in Hulunber, Inner Mongolia, China, which has a temperate continental monsoon climate. They categorized the grassland into temperate meadow steppe, temperate steppe, lowland meadow, and mountain meadow. In another study, Wei et al. [26] examined the grassland classification in Three Rivers Source National Park, Qinghai, China and identified swamp meadow, alpine meadow, alpine steppe, and desert steppe as the classification categories. To our best knowledge, large-scale grassland classifications based on IOCSG for alpine regions of China are rarely reported. There also lacks specific grassland thematic products with a broad temporal range and fine temporal frequency in practice, which hinders further insights into the historical condition and long-term succession of grasslands.

When mapping large-scale grassland in alpine regions, a tricky problem is the availability of cloud-free images over a large area. Thanks to GEE, it not only provides global ready-to-use surface reflectance images but also offers various temporal aggregation methods, such as mean, median, and min/max, to composite multi-temporal images. Aiming to generate cloud-free images, an effective strategy is to use the temporal aggregation method for all the available images with cloud masks within a preset time period. Generally, a monthly composition is not adequate and the most popular strategy for compositing an annual cloud free image is to use images acquired over three years [11]. However, this strategy for annual composition cannot maintain the source information of the specific year as much as possible, especially when there are land cover changes among different years or

seasonal changes within a year. Another popular method is seasonal composition, which selects only images between several months from a single year [27] or multiple years [28] for composition. Seasonal composition can normally achieve a higher land cover classification accuracy than annual composition because of the seasonality of typical land cover types such as grasslands, trees, farmland, etc. [11]. However, the phenology information is not well considered. Thus, an effective image composite method should be further explored for accurate large-scale grassland classification with a high temporal frequency.

Considering the above-mentioned context, the aim of this study is to produce the annual grassland classification products at 30 m from 1986 to 2020 based on IOCSG for the Qinghai province of China, a grassland-dominated province in the alpine region of China, and explore its long-term grassland transitions. Our main contributions include:

- We proposed a methodological framework for the large-scale grassland classification of alpine regions with broad temporal cover and fine temporal frequency.
- We generated a public dataset composed of 35 annual grassland thematic images of Qinghai from 1986 to 2020 at 30 m. The dataset can be fetched from https://drive.google.com/file/d/1TtkFYnXF0uZsQUy_txX-j50rfeUB521t/view?usp=share_link (accessed on 11 January 2023).
- The grassland transitions of Qinghai from 1986 to 2020 were revealed.

The remainder of this article is organized as follows. In Section 2, we elaborate on the study area, datasets, and methodology used in this article. Section 3 exhibits the results of annual grassland mapping and the grassland transitions in Qinghai during 1986–2020. A discussion is presented in Section 4. The concluding remarks are drawn in Section 5.

2. Materials and Methods

2.1. Study Area

Qinghai is an inland province in northwestern China (Figure 1), bounded by 31°36' N–39°19' N and 89°35' E–103°04' E. Qinghai occupies a land area of 722,300 square kilometers, 60% of which is covered with grassland, breeding nearly 11% of the nationwide grass resources. As part of Qinghai-Tibet Plateau, Qinghai has a plateau continental climate. Qinghai experiences extremely cold winters, along with mild summers and significant diurnal temperature variation. The average annual temperature ranges from approximately −5 to 8 °C. In January, temperatures can vary from −18 to −7 °C, while in July they range between 15 and 21 °C. Rainfall is predominantly observed during the summer season, while winter and spring tend to have very low precipitation. The average altitude of Qinghai is over 3000 m above sea level, with the lowest and highest points at elevations of 1644 m and 6851 m, respectively. Qinghai contains a number of high mountains such as the Kunlun Mountain, Qilian Mountain, and Tanggula Mountain. There is also the headwater of the Yangtze River, Yellow River, and Mekong River, called the Three Rivers Source Region. The Qaidam Basin is located in the northwestern part of Qinghai, one-third of which is desert. According to the IOCSG and the Code of Practice for Grassland Resource Survey of the Ministry of Agriculture and Rural Affairs of China (NY/T 2998-2016) [29], the grassland in Qinghai can be classified as nine categories including AM, AS, AMS, AD, LM, MM, TS, TD, TDS. The social economy of Qinghai has experienced rapid growth thanks to national strategies like the Great Western Development and the 'Belt and Road' initiative. This progress has led the province to pursue a sustainable development path, aligning the social economy with the eco-environment [30].

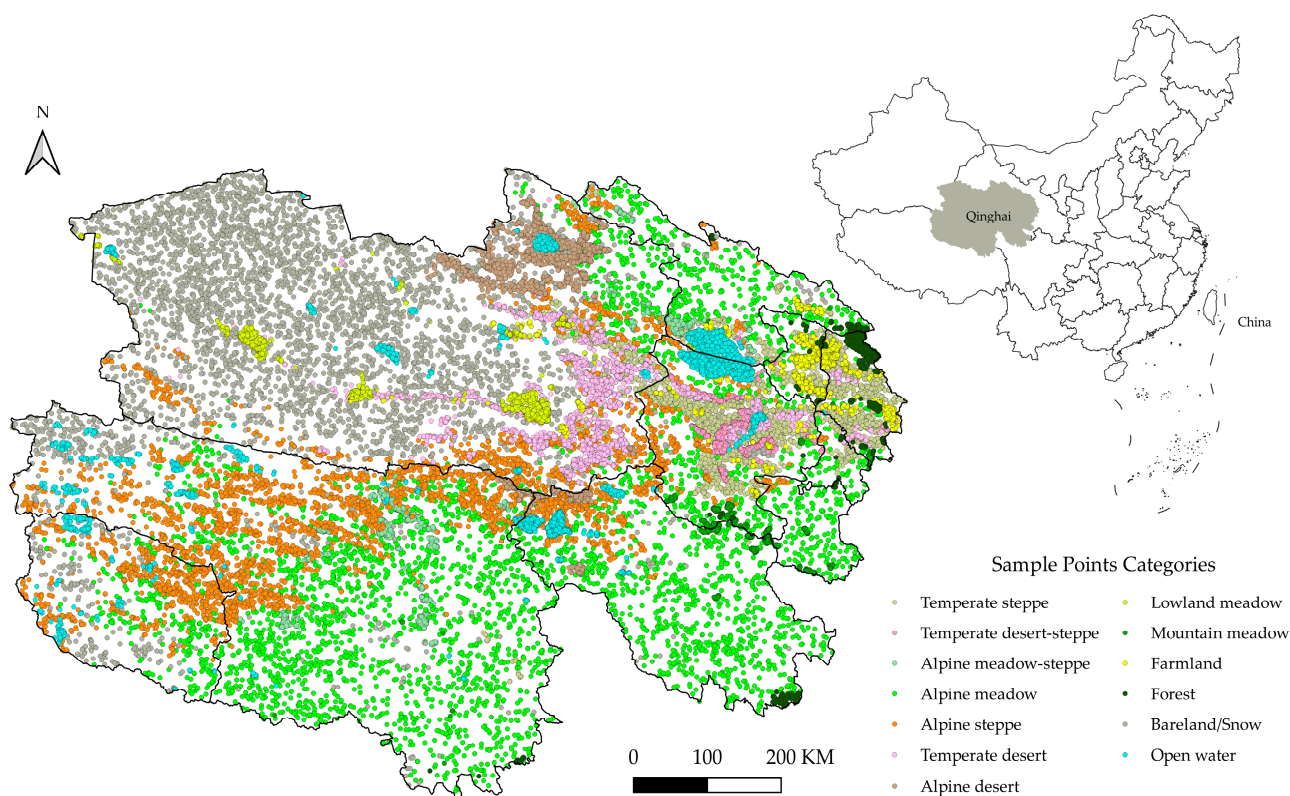


Figure 1. Study area and distribution of sample points.

2.2. Datasets

The datasets used in this study are listed in Table 1; they are elaborated individually in the following subsections.

Table 1. Datasets used in this study.

Dataset	Time Span	Scale	Provider
Landsat surface reflectance images (Landsat 5, 7, 8)	1986–2020	30 m	NASA/USGS
Digital elevation model (SRTM DEM)	2000	30 m	NASA
Grassland thematic map (QGLM)	2011	1:1,000,000	the Geomatics Center of Qinghai
Land cover data (World Cover 10)	2020	10 m	ESA
Impervious surface (GISD30)	every five years from 1985 to 2020	30 m	Zhang et al. [31]

2.2.1. USGS Landsat Surface Reflectance

Among global satellite programs, the NASA/USGS Landsat program has provided the longest continuous space-based record of Earth's land surface since 1972. The fifty year archives of Landsat Earth observations supply the world with an unparalleled view of global change [12,32]. Because of the fine spatial resolution and broad temporal coverage, Landsat datasets are considered an ideal data source for the long-term, large-scale monitoring of grasslands. Landsat scenes with the highest available data quality are placed into Tier 1 and are considered suitable for time-series analysis. Tier 1 includes Level-1 Precision and Terrain (L1TP) corrected data that have well-characterized radiometry and are inter-calibrated across the different Landsat instruments [33]. Considering the large extent and high temporal frequency of this study, we used all available Landsat Collection 2 Tier 1 surface reflectance (SR) products from Landsat 5 Thematic Mapper (TM), Landsat 7 Enhanced Thematic Mapper Plus (ETM+), and Landsat 8 Operational Land Imager (OLI) during 1986–2020. Figure 2 shows the distribution of Landsat Worldwide Reference

System-2 (WRS-2) paths (131~140) and rows (33~38) that cover the geographical region of Qinghai; the total number of image frames is 50.

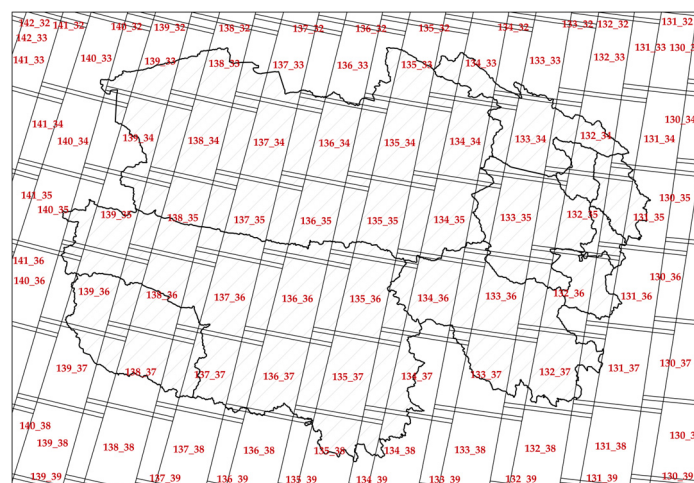


Figure 2. Landsat WRS-2 codes of Qinghai.

2.2.2. Digital Elevation Model (DEM) Data

The temperature and precipitation in Qinghai are spatially heterogeneous, along with different terrains. Consequently, altitude largely determines the distribution of different grassland classes in relation to temperature and humidity. We used The Shuttle Radar Topography Mission (SRTM) DEM [34] as a feature band for classification, which is directly available on GEE. The SRTM DEM is an international research project that has produced DEM at 30 m resolution almost worldwide.

2.2.3. Referenced Grassland Thematic Map and Land Cover Data

In this study, the 2011 grassland thematic map of Qinghai (QGLM 2011) at a scale of 1:1,000,000, authorized by the Geomatics center of Qinghai, was uploaded to GEE; it was used to identify training and testing samples for the classifier. The thematic information of QGLM 2011 includes nine grassland classes from the IOCSG and four land cover classes such as farmland, open water, forest, and bare land/snow (in accord with the sample point categories in Figure 1). At the same time, to mitigate the ambiguity of class boundaries in QGLM 2011, the ESA World Cover 10 m 2020 product [25] with a finer resolution (10 m) was applied to constrain samples selected from QGLM 2011 in accord with the land cover type from the ESA World Cover 10 m 2020 by taking their intersections.

2.2.4. Impervious Surface Data

Due to the absence of impervious surface (IS) samples from QGLM 2011, as well as the spectral complexity of IS, the existing IS product GISD30 [31] was adopted to directly update the annual classification result. GISD30 is a global IS dataset that reflects every five year IS dynamics from 1985 to 2020 in each $5^{\circ} \times 5^{\circ}$ geographical tile. The IS dynamics at an interval of five years are designated with a label ranging from one to eight correspondingly, and the every five year IS maps can be further generated by progressively masking the labelled regions. Eight geographical tiles of IS maps with a longitude code of E85 to E100 and a latitude code of N35 to N40 were mosaiced and uploaded to GEE. The IS maps, updated every five years, were ultimately utilized as masks to revise the grassland classification outcomes by designating the masks as IS. Consequently, the classification system for grassland mapping in Qinghai encompassed a total of fourteen categories, comprising the previously mentioned nine grassland classes and four land cover classes.

2.3. Methodology

Figure 3 illustrates the methodological framework of annual grassland classification of Qinghai from 1986 to 2020, which consists of three major components: annual image composition, classifier training, and annual grassland mapping. In the first part, the annual source images were prepared by quarterly compositing multi-sensor and multi-temporal Landsat surface reflectance images. Then, a Random Forest (RF) classifier was trained according to the composite image of the year 2011 and its referenced grassland thematic map. The final component involves the generation of annual grassland maps from 1986 to 2020 by applying the trained classifier and post-classification processes. Detailed information on the procedures of annual grassland classification will be presented in subsequent sections.

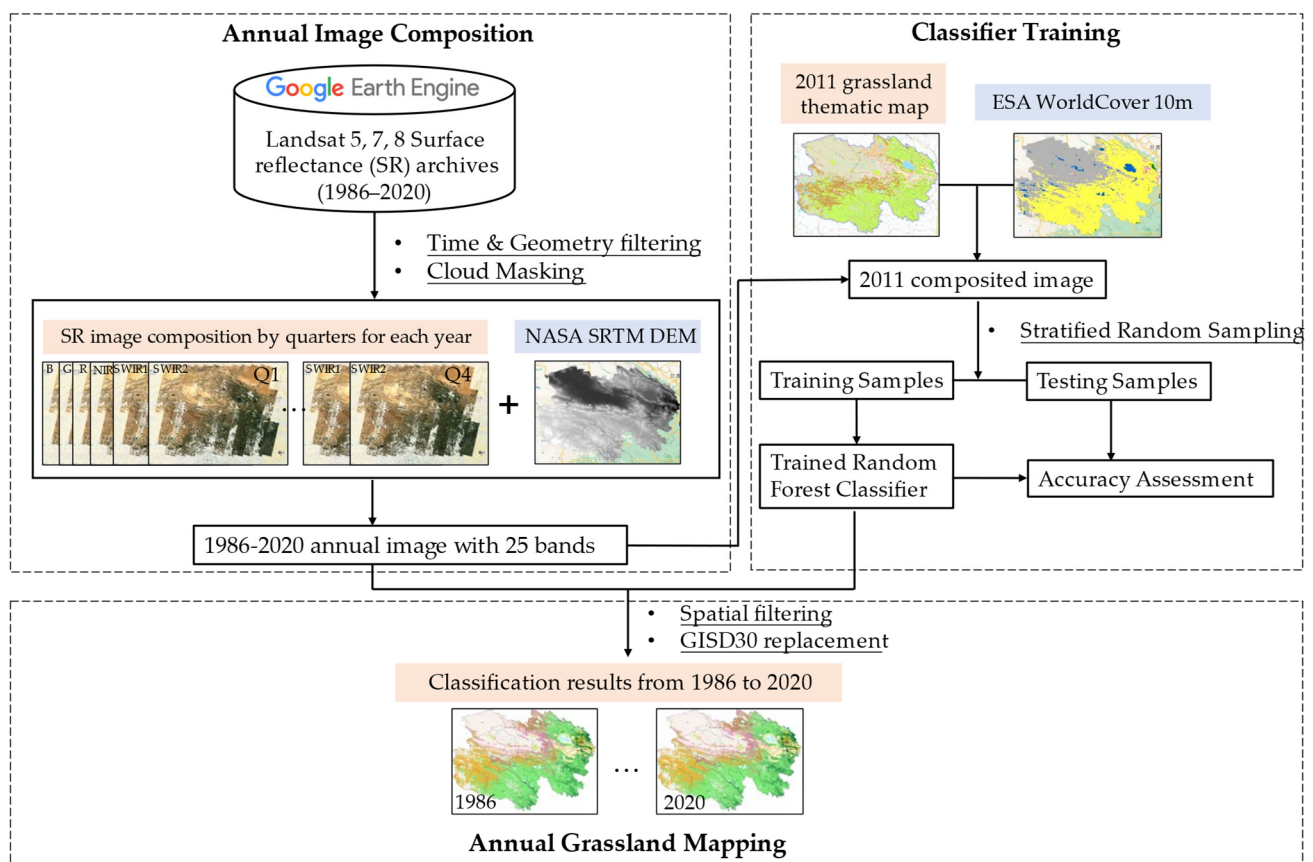


Figure 3. Methodological framework of annual grassland classification from 1986 to 2020.

2.3.1. Annual Image Composition

The high temporal frequency, wide geographic coverage, and frequent cloud cover makes it difficult to map the grassland of Qinghai annually from 1986 to 2020. Thus, we made full use of all Landsat archives by compositing multi-sensor, multi-temporal images covering the 50 frames through the GEE platform. Table 2 lists the available Landsat satellites for each year according to their different service periods and GEE archives.

Table 2. Available Landsat satellite for image composition during 1986 to 2020.

Year	Available Satellite
1986–1998	Landsat 5
1999–2012	Landsat 5, 7
2013–2020	Landsat 7, 8

In a specific year, the available SR data from Landsat 5, 7, and 8 were first filtered based on the given year and the boundary of Qinghai. At the same time, the corresponding bands of multi-sensors were selected, including blue band (B), green band (G), red band (R), near-infrared band (NIR), and two shortwave infrared bands (SWI1, SWI2). Then, the QA_PIXEL band, which indexes the pixel quality attributes from the C Function of Mask (CFMASK) [35] algorithm, was employed to mask dilated clouds, clouds, and cloud shadows. Subsequently, the annual image collection was reduced quarterly by a statistical median reducer on GEE for images dated from January to March, April to June, July to September, and October to December, respectively. The obstinately masked pixels in the annual image collection can be filled by the median value of pixels from the neighbored two years. In this way, the Landsat archives are fully utilized to fill in the missing data due to cloud masks and striping problems of the Landsat-7 sensor. At the same time, the successive seasonal spectrum information has also been integrated into the final annual composite image. Finally, the terrain data, namely SRTM DEM, was added as a band. Each final annual image consists of 24 spectral bands (6 spectral bands per quarterly composite image) and a DEM band, namely, 25 bands in total. They were used as input features for subsequent grassland classification.

The effectiveness of the proposed annual image composition method was verified in terms of two aspects. One is the percentage of invalid data in the final composite image. Taking the third quarter from July to September for example, the composite image based on the proposed strategy was compared to the composite image from a single Landsat sensor. The other aspect is the accuracy of final classification result based on the composite image. Similarly, the quarterly composite of the year was compared to the composite image of the third quarter. In addition, the accuracies of whether considering the elevation information or not for both the two cases were also compared.

2.3.2. Classifier Training

In this study, the training and testing samples were taken from the 2011 annual image using the QGLM 2011 as a reference map. As shown in Figure 1, thirteen classes of the designed classification system (except for IS) were sampled from QGLM 2011 based on stratified random strategy. Each class has four thousand samples and they were split into training and testing samples at 7:3. The inter-class spectral separability among the thirteen classes were further analyzed based on the Jeffries–Matusita (JM) distance [36], which ranges from 0 to 2 with increasing inter-class separability. The Random Forest classifier has been used in many large-scale classification tasks on GEE owing to its reliability [37–39]. We trained an RF classifier with one hundred trees based on the training samples. The performance of the trained RF classifier was evaluated by commonly used metrics such as user's accuracy (UA), producer's accuracy (PA), overall accuracy (OA), and kappa coefficient. These metrics are calculated based on a confusion matrix, which is a table that provides statistics on the number of predicted and actual labels of the testing samples from QGLM 2011.

2.3.3. Annual Grassland Mapping

In this study, the referenced grassland samples are limited and only samples from QGLM 2011 are available. A lack of historical reference samples is a common problem when conducting large-scale and long-term land cover classification. A previous study by Gong et al. [40] successfully transferred a global training sample set developed in 2015 at 30 m resolution to classify 10 m resolution images acquired in 2017 with a sensor on board a different satellite, using RF as the classifier. Experiment results from [40] indicated that the classification result using the RF classifier in global land cover mapping is still stable at a 1% loss of overall accuracy even if there are 60% fewer sample points, the land cover changes by 20%, or the training samples contain a 20% error. Similar research can also be seen in urban land classification [41] and land cover mapping at a regional scale [42]. Moreover, the surface reflectance images from different Landsat instruments have well-characterized

radiometry and are inter-calibrated [33]. Thus, the same strategy was adopted due to the absence of historically referenced grassland samples. We transferred the RF classifier trained on training samples from QGLM 2011 (Section 2.3.2) to the classification of the other years' annual composite images from 1986 to 2020. In terms of post-classification processing, a majority spatial filter with a 3×3 window was used to replace isolated pixels with the mode of surrounding pixels' labels. The final annual thematic map was produced by updating the classification result every five years with IS masks generated based on GSD30.

2.3.4. Grassland Transition Analysis

Once the annual grassland classification data are generated, grassland transition in Qinghai can be further analyzed. We first counted the area of each thematic class over 35 years and a time series decomposition method named Seasonal and Trend decomposition using Loess (STL) [43] was used to obtain the trend item for each thematic class. Subsequently, we calculated the transition matrix among different grassland classes from 1986 to 2020 in order to obtain the quantitative statistics of changes for each thematic class in terms of area and percentage. For each thematic class, the changed area is calculated by subtracting area in 2020 from area in 1986; the changed percentage is calculated by dividing the absolute value of area change by the area in 1986. In addition, the spatial distribution of the changes of AM, AS, and bareland/snow were illustrated as they cover the most land surfaces in Qinghai.

3. Results

3.1. Annual Grassland Mapping

The separability among different grassland classes and the feature importance of the 25 bands for the RF classifier were firstly investigated in this study. Figure 4 illustrates the JM distance matrix for the 13 classes and demonstrates the measures of separability between every two grassland classes. As a whole, the JM distance of most pairs of classes is greater than 1.90, which means the majority of grassland classes in Qinghai have strong separability in terms of the 25 bands. Meanwhile, the JM distance between TD and TS is smaller at 1.708 and AS and AM have the smallest JM distance at 1.487.

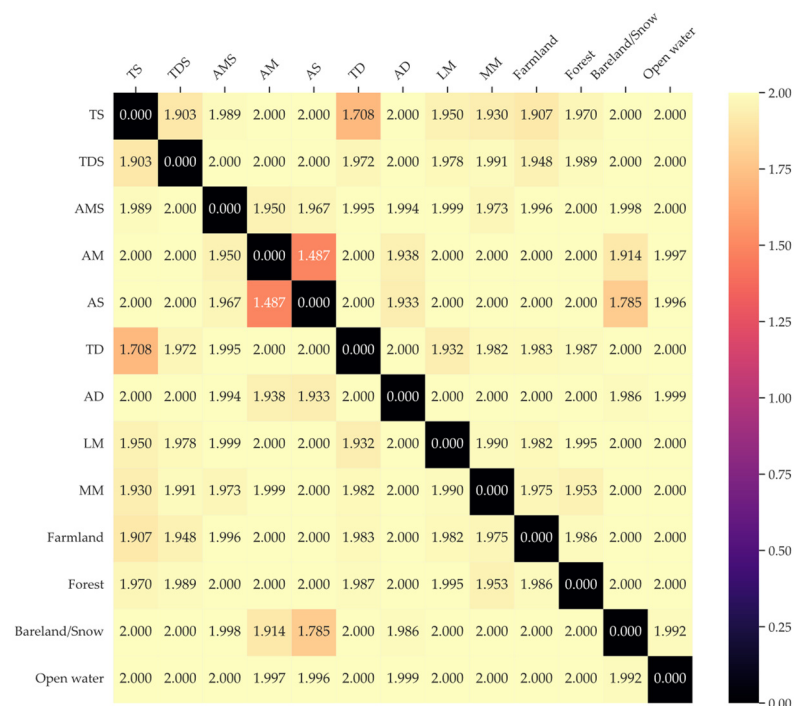


Figure 4. JM distance matrix of the thirteen sampled classes.

Figure 5 shows the feature importance of the 25 bands when the RF classifier was trained. It shows that the elevation and the Q3_NIR band are of remarkable importance during the classification. The NIR, SWI1, and SWI2 bands in the second and third quarters, i.e., from April to September, are more important than other quarters. These facts indicate that the elevation and infrared bands during the grass growing period are vital factors to distinguish different classes when training an RF classifier.

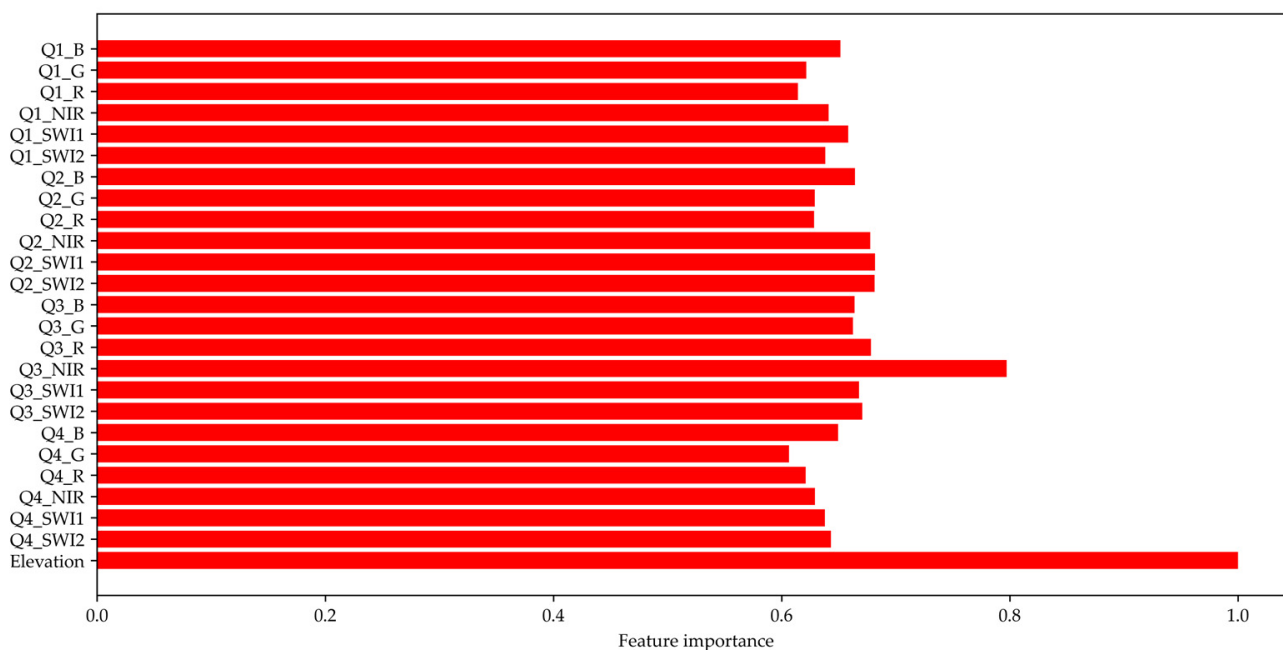


Figure 5. Feature importance of RF classifier.

Figure 6 illustrates the classification result of a composite image of Qinghai in 2011; the result was quantitatively evaluated by testing samples. Table 3 presents the confusion matrix providing statistics on the number of predicted (Prediction) and actual labels (Truth) of the testing samples from QGLM 2011. As a whole, the classifier achieved an overall accuracy at 0.892 and the kappa coefficient is 0.883. Most thematic classes received a user accuracy (UA) and producer accuracy (PA) above 0.90. It is worth noting that the PA and UA are relatively lower for alpine meadow, alpine steppe, temperate desert, and temperate steppe, which is in accord with the inter-separability analysis we discussed in Figure 4. As shown in Figure 6, the Qinghai 2011 grassland mapping accurately shows the distribution of the different grassland classes. Overall, the grassland exhibits a horizontal zonation ranging from the warm and humid southeast to the dry and cold northwest, with a sequence of alpine meadow, alpine steppe, desert steppe, and alpine desert that include sand dunes [44]. Three detailed regions of the Qinghai 2011 grassland map with different landscapes, denoted as A, B, and C in Figure 6, are presented in Figure 7. Figure 8 depicts the corresponding regions every five years during 1995–2020. The results have shown fine classification results of intricate grasslands, finespun rivers, as well as dilated IS regions from GISD30.

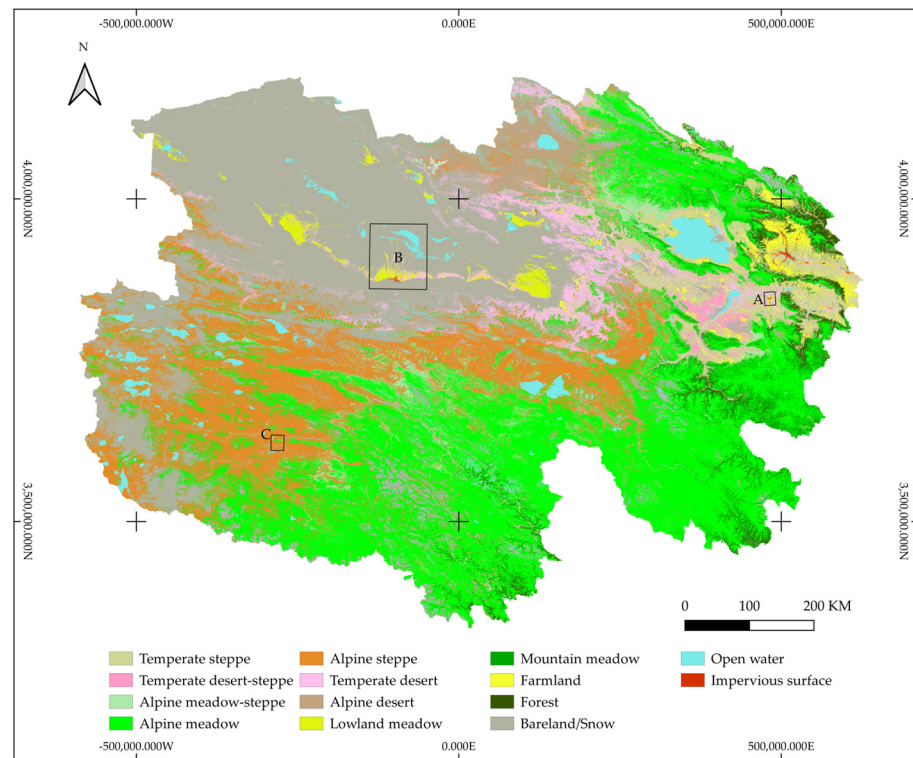


Figure 6. Qinghai grassland mapping in the year 2011 (Georeference: WGS-84, Projection: Albers Equal Area Conic, central meridian: 96° E, 1st standard parallel: 27° N, 2nd standard parallel: 45° N, unit: m). A, B and C represent the exemplified regions demonstrated in Figures 7 and 8. Crosses represent the coordinate grid.

Table 3. Accuracy assessment for grassland mapping of Qinghai in 2011¹.

	Prediction														
	TS	TDS	AMS	AM	AS	TD	AD	LM	MM	Farmland	Forest	Bareland/Snow	Open Water	PA	
Truth	TS	913	91	19	18	2	111	4	4	8	41	11	5	0	0.744
	TDS	40	1164	2	1	0	10	0	0	0	2	0	1	0	0.954
	AMS	2	2	1085	70	46	0	0	0	0	0	0	1	0	0.900
	AM	14	4	83	788	126	11	14	0	70	3	15	12	0	0.691
	AS	40	8	71	52	877	69	54	0	3	1	0	25	0	0.731
	TD	63	14	1	2	31	992	20	34	1	1	2	18	0	0.841
	AD	0	0	10	5	42	15	1165	0	0	0	0	5	0	0.938
	LM	2	0	0	0	0	10	0	1126	0	1	0	3	1	0.985
	MM	5	0	0	10	0	0	0	0	1141	0	4	0	0	0.984
	Farmland	26	1	0	0	0	4	0	4	0	1183	1	0	0	0.970
	Forest	7	0	0	1	0	1	0	0	5	2	1192	0	0	0.987
	Bareland/Snow	2	0	3	9	58	26	28	6	0	0	0	966	5	0.876
	Open water	1	0	0	1	0	2	0	0	0	0	1	5	1190	0.992
	UA	0.819	0.907	0.852	0.823	0.742	0.793	0.907	0.959	0.929	0.959	0.972	0.928	0.995	
Overall Accuracy: 0.892			Kappa: 0.883												

¹ TS: temperate steppe, TDS: temperate desert-steppe, AMS: alpine meadow-steppe, AM: alpine meadow, AS: alpine steppe, TD: temperate desert, AD: alpine desert, LM: lowland meadow, MM: mountain meadow.

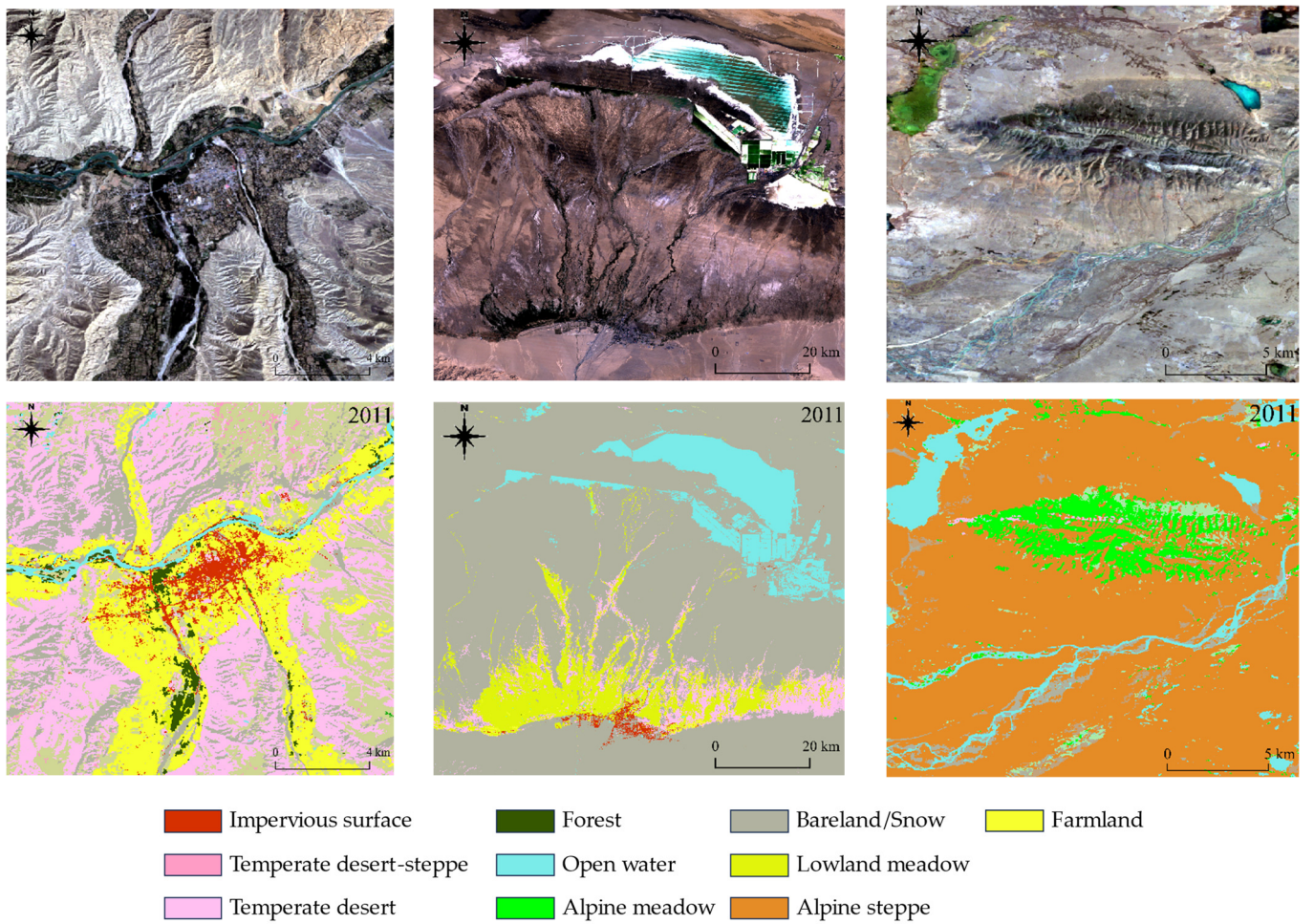


Figure 7. Detailed regions A, B, C (from left to right) in Qinghai grassland map of 2011.

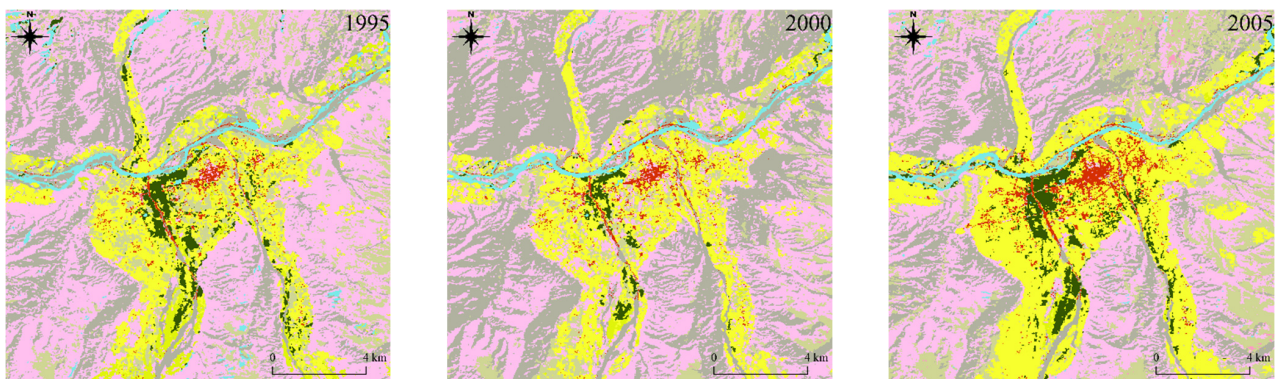


Figure 8. Cont.

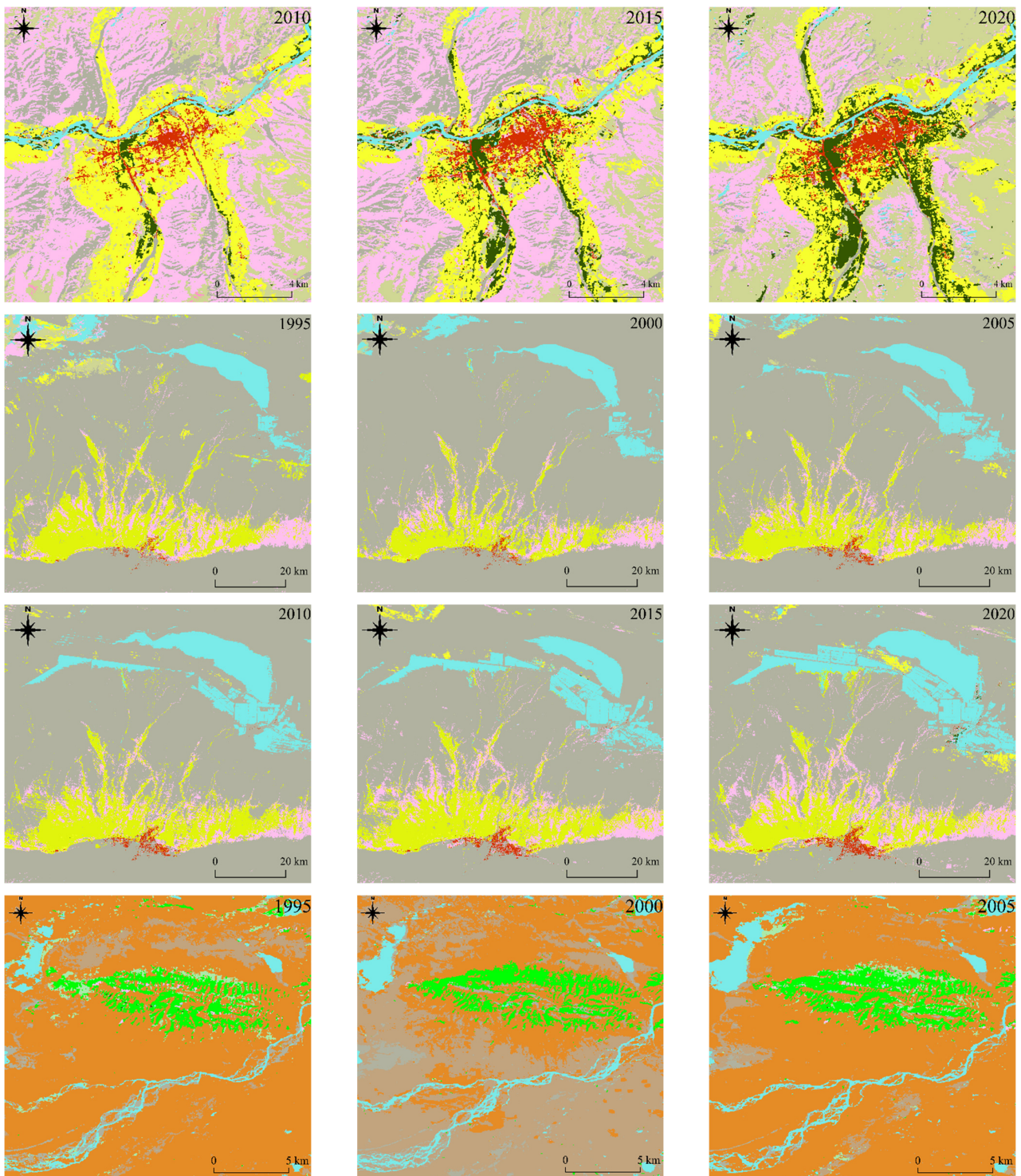


Figure 8. Cont.

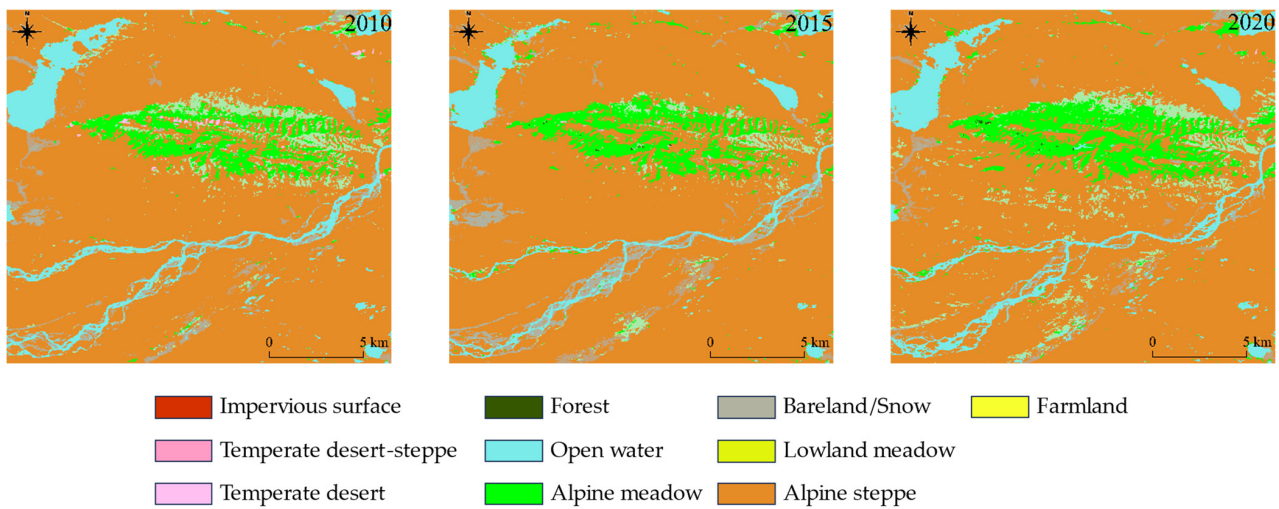


Figure 8. Detailed regions A, B, and C (from up to down) of Qinghai grassland map every five years during 1995–2020.

Moreover, the effectiveness of the proposed annual image composition method was further verified according to the scheme in Section 2.3.1. On the one hand, Table 4 shows the percentage of invalid data in the quinquennial composite image obtained by compositing single Landsat satellite sensor images from July to September and by the proposed strategy from the same period. It is apparent that all the composite images with the proposed strategy hold a significantly low ratio of invalid data, which ensures the integrity of the grassland classification results to a large extent. On the other hand, Figure 9 illustrates the effects of different image composite strategies on classification accuracy. As seen in Figure 9, if the 2011 annual composite image only has spectrum information during July to September (noted as the composite of the third quarter), the overall accuracy and kappa coefficient is the lowest, at 0.814 and 0.798, respectively. Nevertheless, the quarterly composite of the whole year with temporal features of grassland spectrum achieved an overall accuracy and kappa coefficient at 0.870 and 0.859, respectively. It is notable that elevation is an important feature in Qinghai grassland classification (see Figure 5); the integration of elevation information has also greatly promoted the classification accuracy for both the foregoing two cases. The proposed strategy achieved the highest overall accuracy and kappa coefficient at 0.892 and 0.883, respectively.

Table 4. Percentages of invalid data in the different composite images during Jul.-Sept.

Year	Landsat 5	Landsat 7	Landsat 8	The Proposed Composite Image
1990	10.011%	\	\	0.462%
1995	12.048%	\	\	0.026%
2000	3.026%	12.935%	\	0.0003%
2005	11.451%	12.347%	\	0.006%
2010	4.665%	11.598%	\	0.002%
2011	4.534%	11.738%	\	0.006%
2015	\	3.774%	1.331%	0.001%
2020	\	3.481%	4.493%	0.003%

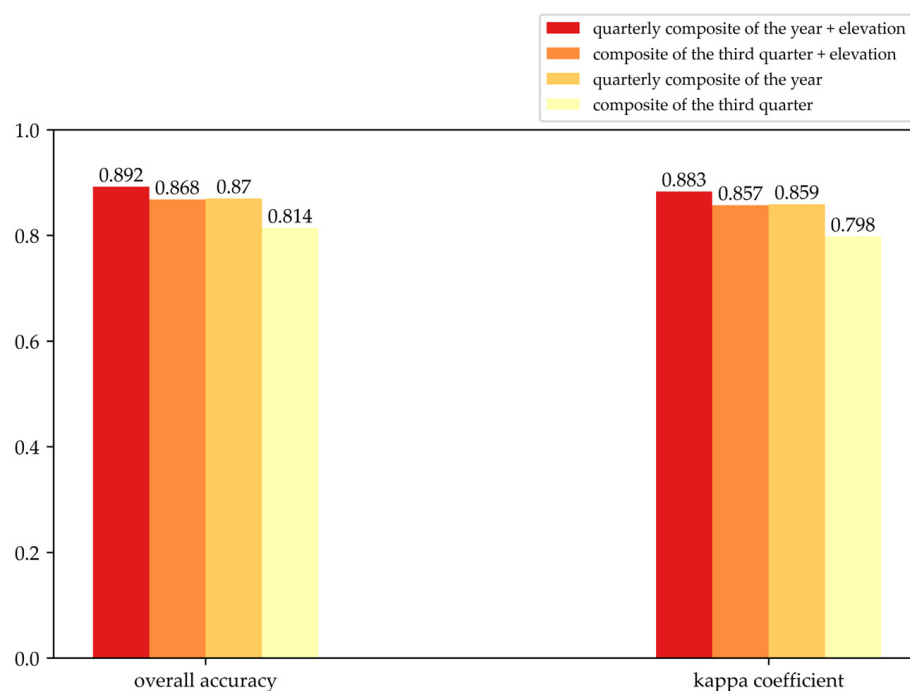


Figure 9. Effects of different image composite strategies on classification accuracy.

3.2. Qinghai Grasslands Transition during 1986–2020

With the 35-year grassland mapping products of Qinghai, the grassland transition can be further analyzed. Figure 10 shows a batch of 35-year area time series for different thematic classes. As shown in Figure 10, the area of IS and bareland/snow shows a persistent trend of rise and decline, respectively. Meanwhile, it can be found that the areas of most thematic classes such as TS, TDS, AMS, AM, AS, TD, MM, farmland, and forest have experienced apparent increases around the year 2000. While around the same year, the AD, LM, and open water came across a decrement. From 2016 to 2020, the areas of AMS, AS, MM, and TDS showed a trend of decline of various extents. The areas of AD, forest, open water, and AM have shown a clear growth trend. TS, TD, LM, and farmland maintained a stable situation over a longer historical period since the year 2000.

Figure 11a,b presents quantitative statistics of change for each thematic class during the 35 years in terms of area and percentage, respectively. Figure 12 is a stacked bar chart of the thematic classes in 2020; each bar exhibits the proportional contribution of different thematic classes from 1986. Figure 13 demonstrates more detailed transitions of classes in Qinghai from 1986 to 2020 with a Sankey diagram. Seen from Figure 11, it is eye-catching that the area of IS has increased by 281.9% during the 35 years. Meanwhile, the areas of AMS, AS, MM, and bareland/snow have declined by around 30% and the percentage of decline for LM is relatively small at 2.6%. In contrast, the areas of the other nine classes experienced varying degrees of growth; the grassland in Qinghai increased by 46,400 km² in total. As the two dominant grassland classes in Qinghai, the area of AM increased by 56,900 km² at a percentage of 31.4%, while the area of AS decreased by 34,200 km² at a percentage of 28.9%. The forest area also increased by 57%, with 10,400 km².

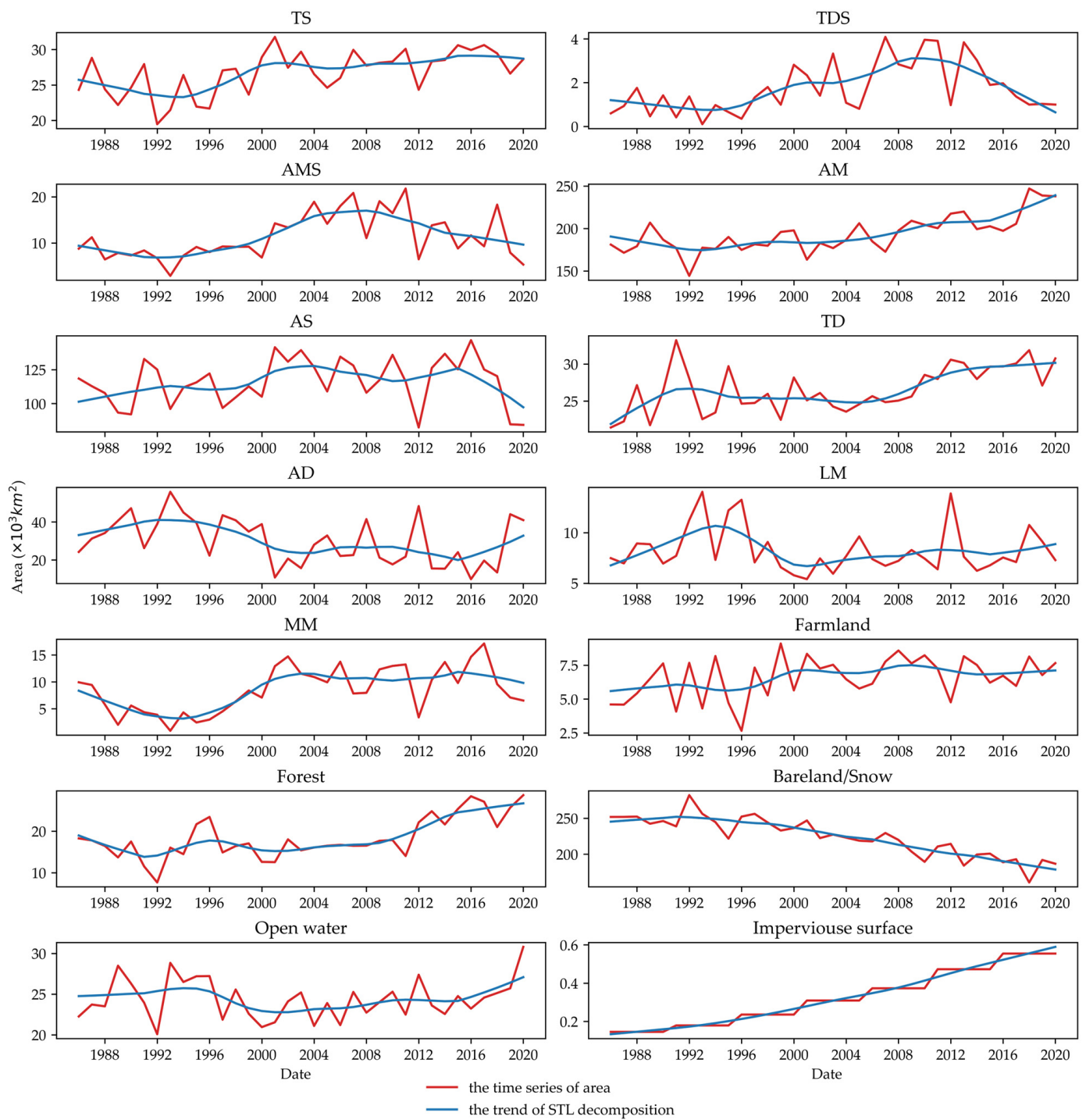
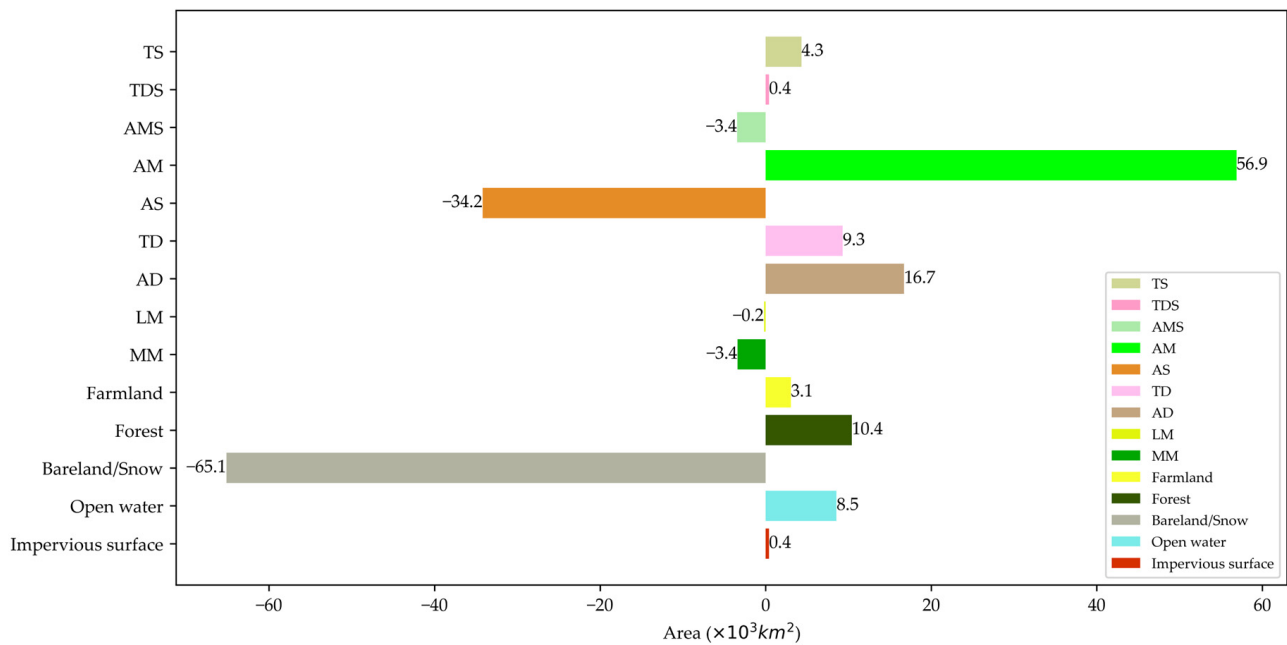
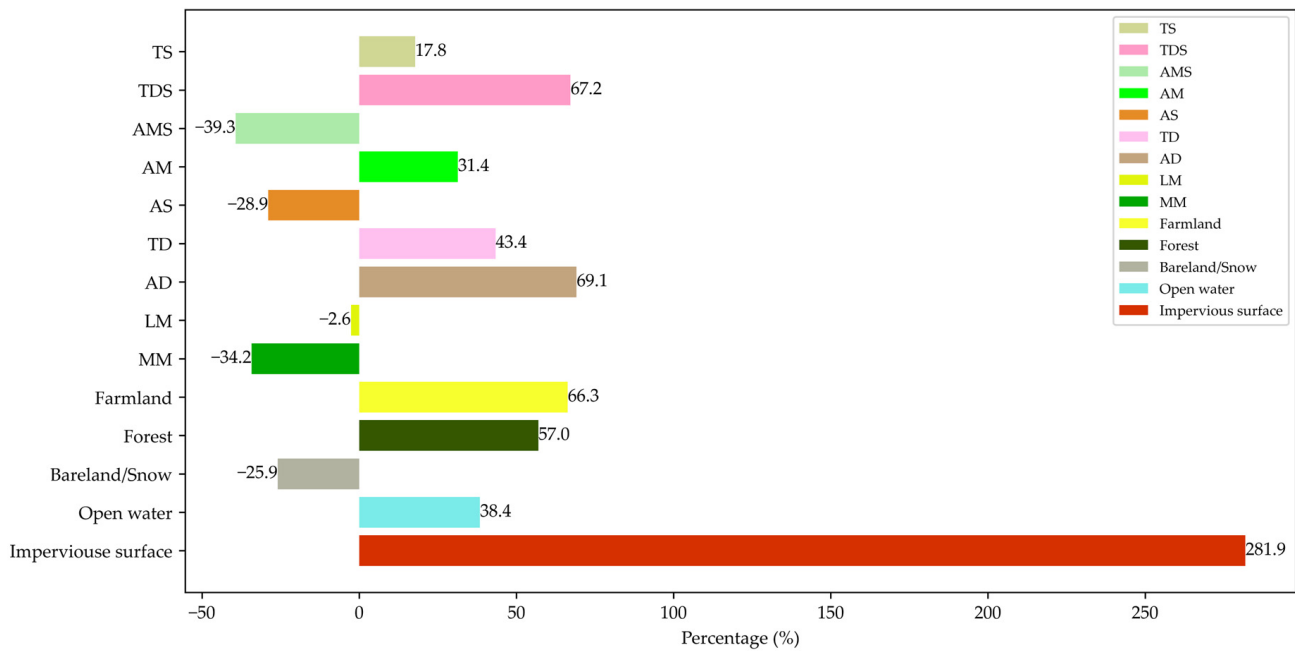


Figure 10. Time series of areas and trends of SLT decomposition for fourteen thematic classes.



(a)



(b)

Figure 11. Area and percentage of change for each thematic class from 1986 to 2020. (a) area of change; (b) percentage of change.

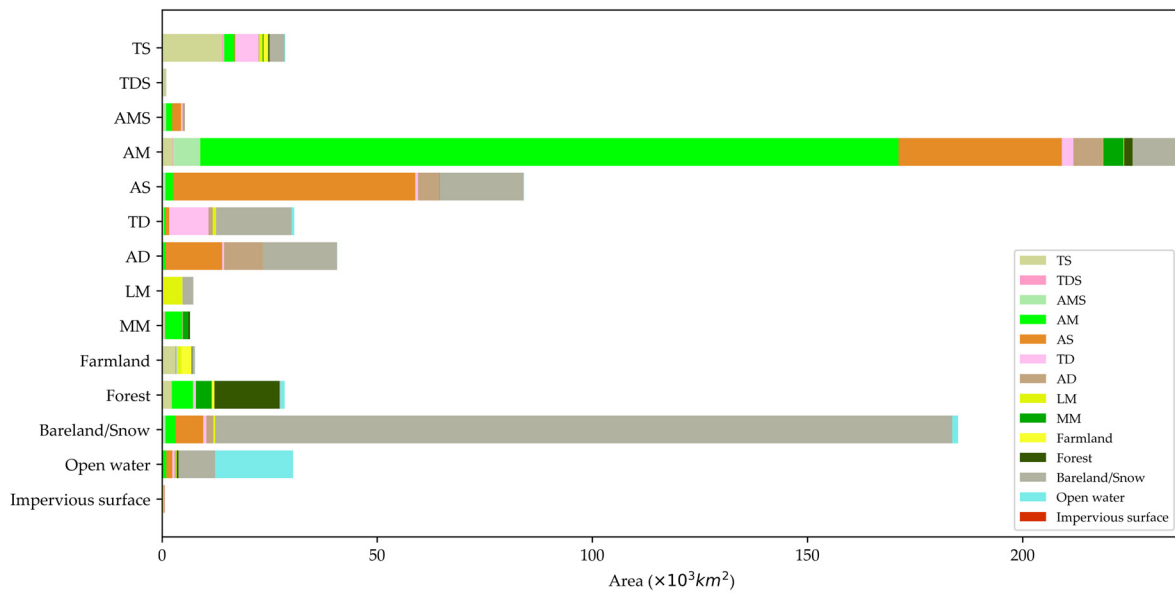


Figure 12. Area of each thematic class in 2020 and transformational contributions of different thematic classes from 1986.

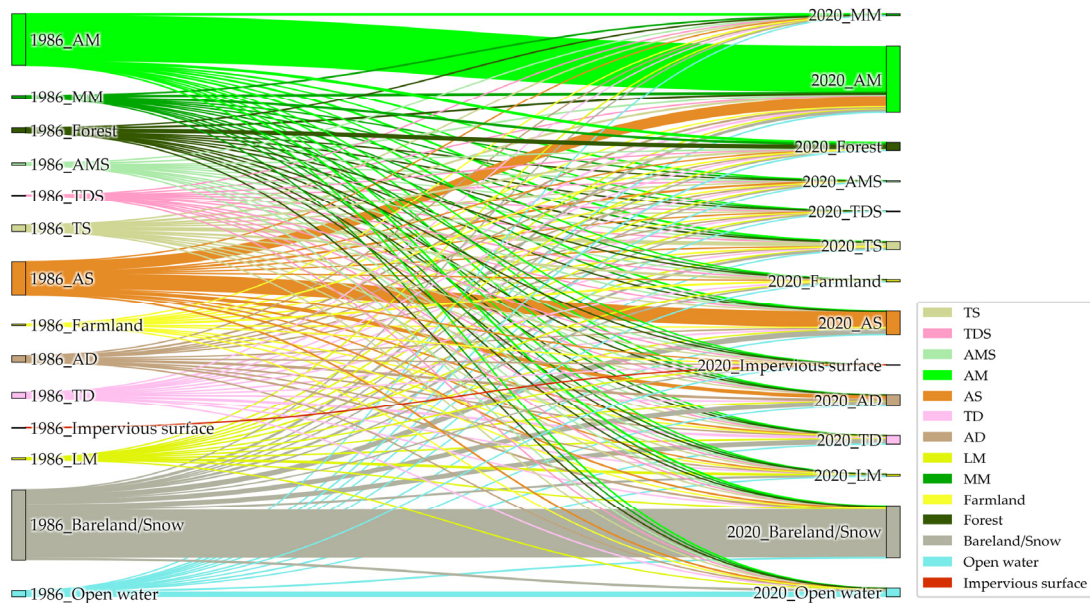


Figure 13. The Sankey diagram of grassland transitions from 1986 to 2020.

As shown in Figures 12 and 13, AM, bareland/snow, and AS are the three largest land surfaces of Qinghai. Notably, the variations in these land surfaces from 1986 to 2020 are particularly significant. In this period, there has been a conversion of approximately 40,000 km² of AS to AM, while around 70,000 km² of bareland/snow has transformed into grasslands such as AM, AS, TD, and AD. The spatial distribution of transitions between AM and AS can be observed in Figure 14a. Primarily, the transformations from AS to AM occurred at the junctions of these two classes. Furthermore, the scope of AM has a trend of expanding westward. The distribution pattern of the bareland/snow decrease from 1986 to 2020 is exhibited in Figure 14b. These changes primarily occurred around the Qaidam Basin, where bareland has undergone a substantial conversion to grasslands. Other reductions in bareland/snow are observed in the southwestern border of Qinghai, encompassing snowcapped high mountains like the Tanggula Mountain. These alterations may be attributable to the melting of snow and ice in these regions.

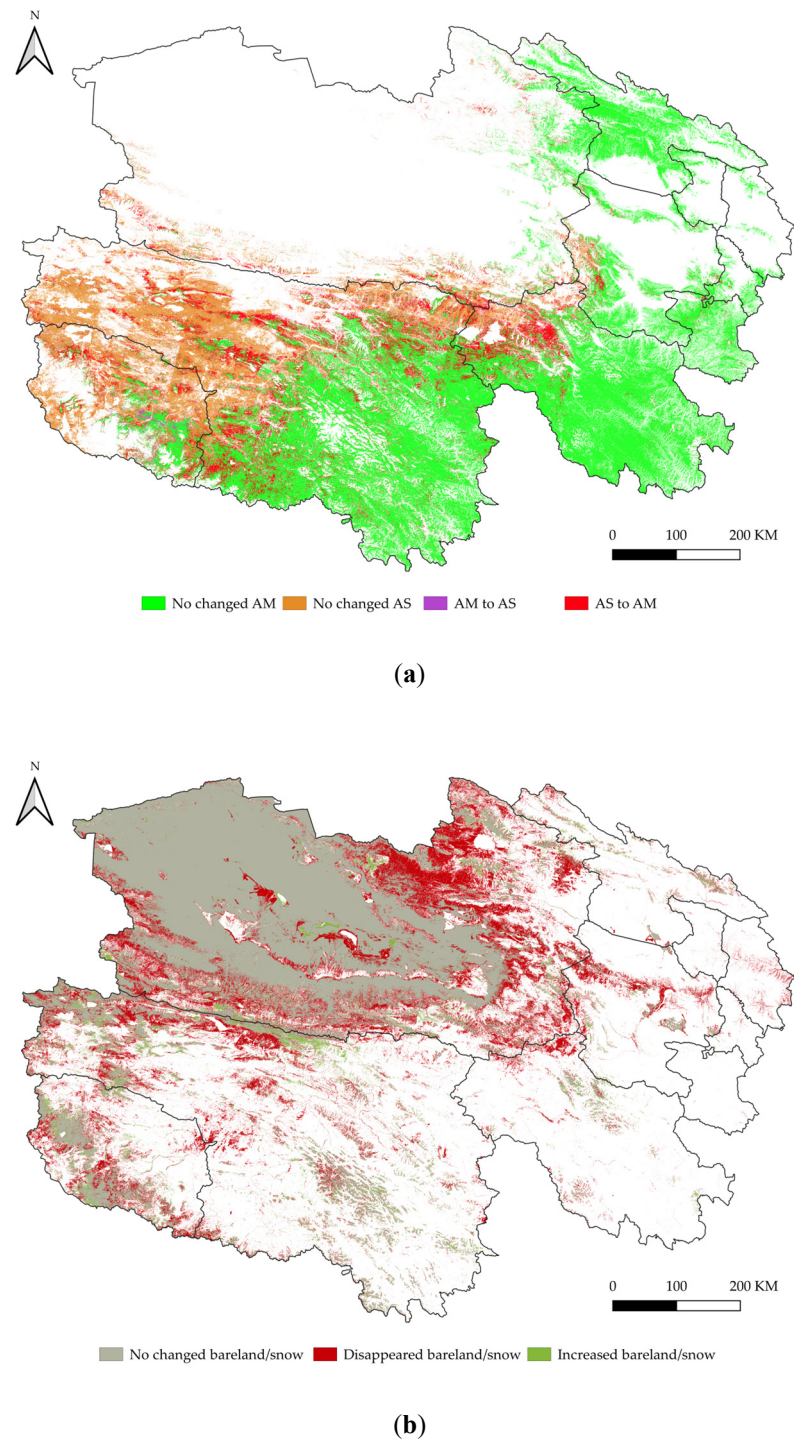


Figure 14. Distribution of changes for typical classes. (a) transitions between AM and AS. (b) changes of bareland/snow.

4. Discussion

4.1. Grassland Mapping of Qinghai

In this study, the classification of the large-scale grassland of Qinghai in terms of the IOCSG was comprehensively investigated by means of remote sensing.

The IOCSG is a grassland classification system proposed by Ren et al. [6] in the 1960s; it has been commonly used in the practice of grassland classification for the past several decades in China. The IOCSG determined the first-level class of grassland by using the $>0\text{ }^{\circ}\text{C}$ annual accumulated temperature and moisture index [6]; thus, it can be utilized to

classify grassland according to climate materials. For example, Wei et al. [45] analyzed the changing characteristics of thermal and moisture conditions over the past 30 years in Inner Mongolia and illustrated the distribution and spatiotemporal variation in grassland types based on the IOCSG. However, the classification result tends to be imprecise because of the coarse resolution of climate data, typically reported at a kilometer level. This study successfully utilized Landsat data at a 30 m resolution to conduct grassland classification in terms of IOCSG. The JM distance among nine grassland classes and four land cover classes (Figure 4) indicated the feasibility of classifying these classes with the designed 25 feature bands. In addition, the feature importance analysis for the trained RF classifier suggested that the elevation and infrared bands during the grass growing period are vital factors to distinguish different classes when training an RF classifier; this is further verified by the accuracy comparison of different composite strategies in Figure 9. Utilizing the composite image of only the third quarter can achieve a classification overall accuracy at 0.814. Elevation can further promote the accuracy for either a composite image of the third quarter or a quarterly composite image of a year.

When mapping large-scale grassland in alpine regions, it is critical to generate annual baseline images for classification facing the challenges of large spatial extent, large time span, high temporal frequency, and heavy cloud cover. When aiming to relieve missing data and cloud masks, a straightforward strategy for a given pixel is to generate a composite value by using satellite observations as much as possible. Phan et al. [11] explored the role of image composition when classifying land cover by using an RF classifier on GEE. Their results show that all images available in a year produce lower accuracy than seasonal image composition and composition images from multiple years' data produce land cover maps with lower accuracy than those from a single year. Different from seasonal composition in [11], our strategy is to generate the quarterly composition of all the available images of a year from multiple Landsat sensors. The effectiveness and advantages of the proposed strategy mainly lie in two perspectives. On the one hand, it can significantly decrease the invalid data in the final composite image (see Table 4). On the other hand, the proposed annual image composition strategy can promote the accuracy of grassland classification by integrating the temporal information of grassland into the final annual composite image (see Figure 9).

The generated annual grassland thematic data in Qinghai from 1986 to 2020 can serve as an elementary dataset for further studies like the vegetation productivity of different grasslands and the response characteristics of different grasslands to climate change. The proposed methodology of large-scale grassland classification can also be referenced to applications like land use/cover mapping and the monitoring of other ecological resources.

4.2. Grassland Transitions in Qinghai

In recent decades, Qinghai has witnessed sustained population growth and the accompanying urban expansion. Warming on the Qinghai-Tibet Plateau has been greater than the global average level [45]. These anthropogenic disturbances and climate change have greatly promoted the possibility of grassland change in Qinghai. The products of Qinghai grassland annual maps from 1986 to 2020 provide a long-term time series dataset for such transition analysis at a 30 m resolution. In general, the area of IS and bareland/snow has kept a persistent trend of rise and decline, respectively, during the 35 years. These observed patterns can be attributed to progressive urbanization and an increased awareness of grassland conservation. Meanwhile, the grassland area of each category in Qinghai exhibits a fluctuating trend under the combined and comprehensive effects of anthropogenic disturbances and climate change. For example, the grassland changes around the year 2000 can be partly interpreted and supported by the alteration of the grassland management policy. According to [46], in the 1980s, the household owned livestock and grazing rights to specified tracts of grassland under the household contract responsibility system. The livestock numbers surged under the loose restrictions on livestock inventories. As a result, there was an alarming degradation of grassland nationwide until the national campaign of

livestock exclusion from grasslands commenced in the early 2000s [47]. A large number of herder families have been moving from the Three Rivers Source Region to centralized resettlement areas and urbanization was continuously promoted (see IS area time series in Figure 10). Prominent warming and wetting in Qinghai-Tibet Plateau since the 1980s has been reported in studies [48,49]. Lou et al. [50] revealed rapid vegetation greening in the changing climate from 1988 to 2018 on the Qinghai-Tibet Plateau. They claimed that precipitation and air temperature are the dominant factors in the greening of the Qinghai-Tibet Plateau and that the greening is mainly a transition from bareland to alpine grassland. This is in accord with our results that the extent of bareland/snow in Qinghai has decreased by 65,100 km² from 1986 to 2020, whereas grasslands have expanded by 46,400 km² during the same period. Additionally, as the IOCSG determine the moisture index (K-value in [6]) of AM is at >1.5 while AS is at 0.9–1.2, the AM tends to be more suitable for humid environments than AS. In our results, there has been a conversion of approximately 40,000 km² of AS to AM. This conversion is also in line with the wetting trend observed in Qinghai.

4.3. Limitations

Uncertainties still exist to some extent in the 35-year Qinghai grassland mapping products on account of the complexity of the Qinghai grassland ecosystem over such a broad geographical and temporal cover, as well as the scarcity of historical reference grassland samples. Additionally, the long-term transition of Qinghai grassland is a result of the comprehensive effects of human activities and climate change. In future studies, we will explore detailed driven factors of grassland transition and its mechanisms in Qinghai in terms of long-term meteorological data.

5. Conclusions

In this work, the large-scale classification of alpine grassland in terms of IOCSG with fine temporal range and frequency was systematically investigated on GEE. A strategy of compositing multi-sensors and multi-temporal Landsat surface reflectance data was designed to obtain baseline images against the difficulties of high temporal frequency, wide geographic coverage, and frequent cloud cover across alpine regions. Annual classification products of grasslands in Qinghai, China, from 1986 to 2020 at 30 m were produced with 14 thematic classes. The quantitative and qualitative analyzes of the results have shown the effectiveness of the proposed methodology. Ultimately, the grassland transitions in Qinghai during 1986–2020 were analyzed. Our main findings include: (1) The different grasslands in Qinghai can be effectively differentiated in terms of the IOCSG by utilizing the designed feature bands of remote sensing data. (2) The proposed image composite strategy can significantly decrease the invalid data and promote classification accuracy. (3) The transitions of grassland in Qinghai from 1986 to 2020 imply the progressive urbanization, warming, and wetting trend in Qinghai.

Author Contributions: Conceptualization, Y.S. and P.H.; methodology, P.H.; validation, P.H.; formal analysis, P.H., Y.S., H.D. and F.Y.; writing—original draft preparation, P.H.; writing—review and editing, P.H., Y.S. and H.D.; project administration, Y.S. All authors have read and agreed to the published version of the manuscript.

Funding: This research was funded by the National Natural Science Foundation of China, grant number U20A2098, and the Natural Science Foundation of Jiangsu Province, grant number BK20190785.

Data Availability Statement: The 35 annual grassland thematic images of Qinghai from 1986 to 2020 at 30m can be fetched from https://drive.google.com/file/d/1TtkFYnXF0uZsQUy_tX-j50rfeUB521t/view?usp=share_link (accessed on 11 January 2023).

Conflicts of Interest: The authors declare no conflict of interest.

References

- Bardgett, R.D.; Bullock, J.M.; Lavorel, S.; Manning, P.; Schaffner, U.; Ostle, N.; Chomel, M.; Durigan, G.; Fry, E.L.; Johnson, D.; et al. Combatting global grassland degradation. *Nat. Rev. Earth Environ.* **2021**, *2*, 720–735. [[CrossRef](#)]
- Bengtsson, J.; Bullock, J.M.; Egoh, B.; Everson, C.; Everson, T.; O'Connor, T.; O'Farrell, P.J.; Smith, H.G.; Lindborg, R. Grasslands—More important for ecosystem services than you might think. *Ecosphere* **2019**, *10*, e02582. [[CrossRef](#)]
- Zhao, Y.; Liu, Z.; Wu, J. Grassland ecosystem services: A systematic review of research advances and future directions. *Landsc. Ecol.* **2020**, *35*, 793–814. [[CrossRef](#)]
- Xu, D.; Chen, B.; Shen, B.; Wang, X.; Yan, Y.; Xu, L.; Xin, X. The classification of grassland types based on object-based image analysis with multisource data. *Rangel. Ecol. Manag.* **2019**, *72*, 318–326. [[CrossRef](#)]
- Liu, H.; Mi, Z.; Lin, L.I.; Wang, Y.; Zhang, Z.; Zhang, F.; Wang, H.; Liu, L.; Zhu, B.; Cao, G.; et al. Shifting plant species composition in response to climate change stabilizes grassland primary production. *Proc. Natl. Acad. Sci. USA* **2018**, *115*, 4051–4056. [[CrossRef](#)] [[PubMed](#)]
- Ren, J.Z.; Hu, Z.Z.; Zhao, J.; Zhang, D.G.; Hou, F.J.; Lin, H.L.; Mu, X.D. A grassland classification system and its application in China. *Rangel. J.* **2008**, *30*, 199–209. [[CrossRef](#)]
- Chen, H.; Zhu, Q.; Peng, C.; Wu, N.; Wang, Y.; Fang, X.; Gao, Y.; Zhu, D.; Yang, G.; Tian, J.; et al. The impacts of climate change and human activities on biogeochemical cycles on the Qinghai-Tibetan Plateau. *Glob. Chang. Biol.* **2013**, *19*, 2940–2955. [[CrossRef](#)] [[PubMed](#)]
- Friedl, M.A.; McIver, D.K.; Hodges, J.C.F.; Zhang, X.Y.; Muchoney, D.; Strahler, A.H.; Woodcock, C.E.; Gopal, S.; Schneider, A.; Cooper, A.; et al. Global land cover mapping from MODIS: Algorithms and early results. *Remote Sens. Environ.* **2002**, *83*, 287–302. [[CrossRef](#)]
- Chaves, M.E.D.; Picoli, M.C.A.; Sanches, I.D. Recent applications of Landsat 8/OLI and Sentinel-2/MSI for land use and land cover mapping: A systematic review. *Remote Sens.* **2020**, *12*, 3062. [[CrossRef](#)]
- Nasiri, V.; Deljouei, A.; Moradi, F.; Sadeghi, S.M.M.; Borz, S.A. Land use and land cover mapping using Sentinel-2, Landsat-8 Satellite Images, and Google Earth Engine: A comparison of two composition methods. *Remote Sens.* **2022**, *14*, 1977. [[CrossRef](#)]
- Phan, T.N.; Kuch, V.; Lehnert, L.W. Land cover classification using Google Earth Engine and random forest classifier—The role of image composition. *Remote Sens.* **2020**, *12*, 2411. [[CrossRef](#)]
- Wulder, M.A.; Roy, D.P.; Radeloff, V.C.; Loveland, T.R.; Anderson, M.C.; Johnson, D.M.; Healey, S.; Zhu, Z.; Scambos, T.A.; Pahlevan, N.; et al. Fifty years of Landsat science and impacts. *Remote Sens. Environ.* **2022**, *280*, 113195. [[CrossRef](#)]
- Gorelick, N.; Hancher, M.; Dixon, M.; Ilyushchenko, S.; Thau, D.; Moore, R. Google Earth Engine: Planetary-scale geospatial analysis for everyone. *Remote Sens. Environ.* **2017**, *202*, 18–27. [[CrossRef](#)]
- Zhang, X.; Liu, L.; Chen, X.; Gao, Y.; Xie, S.; Mi, J. GLC_FCS30: Global land-cover product with fine classification system at 30 m using time-series Landsat imagery. *Earth Syst. Sci. Data* **2021**, *13*, 2753–2776. [[CrossRef](#)]
- Yang, J.; Huang, X. The 30 m annual land cover dataset and its dynamics in China from 1990 to 2019. *Earth Syst. Sci. Data* **2021**, *13*, 3907–3925. [[CrossRef](#)]
- Ji, R.; Tan, K.; Wang, X.; Pan, C.; Xin, L. Spatiotemporal Monitoring of a Grassland Ecosystem and Its Net Primary Production Using Google Earth Engine: A Case Study of Inner Mongolia from 2000 to 2020. *Remote Sens.* **2021**, *13*, 4480. [[CrossRef](#)]
- Zhao, Y.; Zhu, W.; Wei, P.; Fang, P.; Zhang, X.; Yan, N.; Liu, W.; Zhao, H.; Wu, Q. Classification of Zambian grasslands using random forest feature importance selection during the optimal phenological period. *Ecol. Indic.* **2022**, *135*, 108529. [[CrossRef](#)]
- Liu, L.; Xiao, X.; Qin, Y.; Wang, J.; Xu, X.; Hu, Y.; Qiao, Z. Mapping cropping intensity in China using time series Landsat and Sentinel-2 images and Google Earth Engine. *Remote Sens. Environ.* **2020**, *239*, 111624. [[CrossRef](#)]
- Hu, T.; Toman, E.M.; Chen, G.; Shao, G.; Zhou, Y.; Li, Y.; Zhao, K.; Feng, Y. Mapping fine-scale human disturbances in a working landscape with Landsat time series on Google Earth Engine. *ISPRS J. Photogramm. Remote Sens.* **2021**, *176*, 250–261. [[CrossRef](#)]
- Marin, N.A.; Barboza, E.; López, R.S.; Vásquez, H.V.; Gómez Fernández, D.; Terrones Murga, R.E.; Rojas Briceño, N.B.; Oliva-Cruz, M.; Gamarra Torres, O.A.; Silva López, J.O.; et al. Spatiotemporal Dynamics of Grasslands Using Landsat Data in Livestock Micro-Watersheds in Amazonas (NW Peru). *Land* **2022**, *11*, 674. [[CrossRef](#)]
- Yin, S.; Wu, W.; Zhao, X.; Gong, C.; Li, X.; Zhang, L. Understanding spatiotemporal patterns of global forest NPP using a data-driven method based on GEE. *PLoS ONE* **2020**, *15*, e0230098. [[CrossRef](#)]
- Gong, P.; Wang, J.; Yu, L.; Zhao, Y.; Liang, L.; Niu, Z.; Huang, X.; Fu, H.; Liu, S.; et al. Finer resolution observation and monitoring of global land cover: First mapping results with Landsat TM and ETM+ data. *Int. J. Remote Sens.* **2013**, *34*, 2607–2654. [[CrossRef](#)]
- Chen, J.; Chen, J.; Liao, A.; Cao, X.; Chen, L.; Chen, X.; He, C.; Han, G.; Peng, S.; Lu, M.; et al. Global land cover mapping at 30 m resolution: A POK-based operational approach. *ISPRS J. Photogramm. Remote Sens.* **2015**, *103*, 7–27. [[CrossRef](#)]
- Karra, K.; Kontgis, C.; Statman-Weil, Z.; Mazzariello, J.C.; Mathis, M.; Brumby, S.P. Global land use/land cover with Sentinel 2 and deep learning. In Proceedings of the 2021 IEEE International Geoscience and Remote Sensing Symposium IGARSS 2021, Brussels, Belgium, 11–16 July 2021.
- Zanaga, D.; Van De Kerchove, R.; Daems, D.; De Keersmaecker, W.; Brockmann, C.; Kirches, G.; Wevers, J.; Cartus, O.; Santoro, M.; Fritz, S.; et al. ESA WorldCover 10 m 2021 v200. [Data set]. *Zenodo* **2022**. [[CrossRef](#)]
- Wei, Y.; Wang, W.; Tang, X.; Li, H.; Hu, H.; Wang, X. Classification of alpine grasslands in cold and high altitudes based on multispectral Landsat-8 images: A case study in Sanjiangyuan National Park, China. *Remote Sens.* **2022**, *14*, 3714. [[CrossRef](#)]

27. Nyland, K.E.; Gunn, G.E.; Shiklomanov, N.I.; Engstrom, R.N.; Streletskiy, D.A. Land cover change in the lower Yenisei River using dense stacking of landsat imagery in Google Earth Engine. *Remote Sens.* **2018**, *10*, 1226. [[CrossRef](#)]
28. Hu, Y.; Hu, Y. Land cover changes and their driving mechanisms in Central Asia from 2001 to 2017 supported by Google Earth Engine. *Remote Sens.* **2019**, *11*, 554. [[CrossRef](#)]
29. Ministry of Agriculture and Rural Affairs of China. *The Code of Practice for Grassland Resource Survey (NY/T 2998-2016)*; Ministry of Agriculture and Rural Affairs of China: Beijing, China, 2016.
30. Ma, X.; Zhang, H. Variations in the Value and Trade-Offs/Synergies of Ecosystem Services on Topographic Gradients in Qinghai Province, China. *Sustainability* **2022**, *14*, 15546. [[CrossRef](#)]
31. Zhang, X.; Liu, L.; Zhao, T.; Gao, Y.; Chen, X.; Mi, J. GISD30: Global 30 m impervious-surface dynamic dataset from 1985 to 2020 using time-series Landsat imagery on the Google Earth Engine platform. *Earth Syst. Sci. Data* **2022**, *14*, 1831–1856. [[CrossRef](#)]
32. Hemati, M.; Hasanlou, M.; Mahdianpari, M.; Mohammadimanesh, F. A systematic review of landsat data for change detection applications: 50 years of monitoring the earth. *Remote Sens.* **2021**, *13*, 2869. [[CrossRef](#)]
33. Landsat Missions, Landsat Collection 2. Available online: <https://www.usgs.gov/landsat-missions/landsat-collection-2> (accessed on 17 August 2023).
34. Farr, T.G.; Rosen, P.A.; Caro, E.; Crippen, R.; Duren, R.; Hensley, S.; Kobrick, M.; Paller, M.; Rodriguez, E.; Roth, L.; et al. The shuttle radar topography mission. *Rev. Geophys.* **2007**, *45*, 2. [[CrossRef](#)]
35. Foga, S.; Scaramuzza, P.L.; Guo, S.; Zhu, Z.; Dilley, R.D., Jr.; Beckmann, T.; Schmidt, G.L.; Dwyer, J.L.; Hughes, M.J.; Laue, B. Cloud detection algorithm comparison and validation for operational Landsat data products. *Remote Sens. Environ.* **2017**, *194*, 379–390. [[CrossRef](#)]
36. Dabboor, M.; Howell, S.; Shokr, M.; Yackel, J. The Jeffries–Matusita distance for the case of complex Wishart distribution as a separability criterion for fully polarimetric SAR data. *Int. J. Remote Sens.* **2014**, *35*, 6859–6873.
37. Teluguntla, P.; Thenkabail, P.S.; Oliphant, A.; Xiong, J.; Gumma, M.K.; Congalton, R.G.; Yadav, K.; Huete, A. A 30-m landsat-derived cropland extent product of Australia and China using random forest machine learning algorithm on Google Earth Engine cloud computing platform. *ISPRS J. Photogramm. Remote Sens.* **2018**, *144*, 325–340. [[CrossRef](#)]
38. Collins, L.; Griffioen, P.; Newell, G.; Mellor, A. The utility of Random Forests for wildfire severity mapping. *Remote Sens. Environ.* **2018**, *216*, 374–384. [[CrossRef](#)]
39. Srinet, R.; Nandy, S.; Padalia, H.; Ghosh, S.; Watham, T.; Patel, N.R.; Chauhan, P. Mapping plant functional types in Northwest Himalayan foothills of India using random forest algorithm in Google Earth Engine. *Int. J. Remote Sens.* **2020**, *41*, 7296–7309. [[CrossRef](#)]
40. Gong, P.; Liu, H.; Zhang, M.; Li, C.; Wang, J.; Huang, H.; Clinton, N.; Ji, L.; Li, W.; Bai, Y.; et al. Stable classification with limited sample: Transferring a 30-m resolution sample set collected in 2015 to mapping 10-m resolution global land cover in 2017. *Sci. Bull.* **2019**, *6*, 370–373. [[CrossRef](#)] [[PubMed](#)]
41. Li, C.; Wang, J.; Wang, L.; Hu, L.; Gong, P. Comparison of classification algorithms and training sample sizes in urban land classification with Landsat thematic mapper imagery. *Remote Sens.* **2014**, *6*, 964–983. [[CrossRef](#)]
42. Pelletier, C.; Valero, S.; Inglada, J.; Champion, N.; Marais Sicre, C.; Dedieu, G. Effect of training class label noise on classification performances for land cover mapping with satellite image time series. *Remote Sens.* **2017**, *9*, 173. [[CrossRef](#)]
43. Cleveland, R.B.; Cleveland, W.S.; McRae, J.E.; Terpenning, I. STL: A seasonal-trend decomposition. *J. Off. Stat.* **1990**, *6*, 3–73.
44. Kang, L.; Han, X.; Zhang, Z.; Sun, O.J. Grassland ecosystems in China: Review of current knowledge and research advancement. *Philos. Trans. R. Soc. B Biol. Sci.* **2007**, *362*, 997–1008. [[CrossRef](#)] [[PubMed](#)]
45. Wei, P.; Xu, L.; Pan, X.; Hu, Q.; Li, Q.; Zhang, X.; Shao, C.; Wang, C.; Wang, X. Spatio-temporal variations in vegetation types based on a climatic grassland classification system during the past 30 years in Inner Mongolia, China. *Catena* **2020**, *185*, 104298. [[CrossRef](#)]
46. Feng, H.; Squires, V.R. Socio-environmental dynamics of alpine grasslands, steppes and meadows of the Qinghai–Tibetan Plateau, China: A commentary. *Appl. Sci.* **2020**, *10*, 6488. [[CrossRef](#)]
47. Li, L.H.; Xin, X.P.; Tang, H.J.; Hou, L.Y. China’s meadow grasslands: Challenges and opportunities. *Plant Soil* **2022**, *473*, 1–8.
48. Kuang, X.; Jiao, J.J. Review on climate change on the Tibetan Plateau during the last half century. *J. Geophys. Res. Atmos.* **2016**, *121*, 3979–4007. [[CrossRef](#)]
49. Zhang, G.; Nan, Z.; Zhao, L.; Liang, Y.; Cheng, G. Qinghai-Tibet Plateau wetting reduces permafrost thermal responses to climate warming. *Earth Planet. Sci. Lett.* **2021**, *562*, 116858. [[CrossRef](#)]
50. Lou, P.; Wu, T.; Yang, S.; Wu, X.; Chen, J.; Zhu, X.; Ma, X. Deep learning reveals rapid vegetation greening in changing climate from 1988 to 2018 on the Qinghai-Tibet Plateau. *Ecol. Indic.* **2023**, *148*, 110020. [[CrossRef](#)]

Disclaimer/Publisher’s Note: The statements, opinions and data contained in all publications are solely those of the individual author(s) and contributor(s) and not of MDPI and/or the editor(s). MDPI and/or the editor(s) disclaim responsibility for any injury to people or property resulting from any ideas, methods, instructions or products referred to in the content.